

# Analysis of Solvent-Free Intensive-Dry-Mixed NMC-Based Lithium-Ion Battery Cathodes: Numerical Investigations on Performance Determinants

Anshuman Chauhan,<sup>\*[a]</sup> Clemens Lischka,<sup>[a]</sup> and Hermann Nirschl<sup>[a]</sup>

A numerical investigation on the implications of intensive-dry mixing on the resulting cathode microstructure and hence, the electrochemical performance has been presented in this contribution. In this regard, characterization as well as scale-resolving electrochemical performance simulations were carried out. The basis for these numerical investigations were computer generated cathode geometries, generated by means of a discrete element method simulation model, presented in our previous work. Consequently, three different stages of comminution of the conductivity additive during intensive dry mixing with nickel rich active material were incorporated into computational half cells and classified based on the simple quality parameter, bulk density. Furthermore, the possible coating phenomenon occurring during the process, to which the bulk

density measurements are not susceptible, was modelled with the help of a numerical parameter called the coating factor. It was found that bulk density of cathode blends, which is a rather trivial parameter to measure from intensive dry mixed blends, could be strongly correlated to cathode performance under the consideration of solvent free manufacturing. The findings suggest that, while considering limited volume during cell design, higher bulk density of dry cathode components delivers the best performance under higher energy and low current conditions. At high power and high current condition however, a compromise between energy and power dictates the choice. Conversely, if the material mass is the constraining factor, the lower bulk density tends to perform the best due the best utilisation of the available energy.


## 1. Introduction


In the midst of the global push towards sustainable energy sources, the escalating demand for lithium-ion batteries plays a pivotal role in fueling the energy transition. To meet modern energy needs, there is an increasing emphasis on enhancing production as well as performance of batteries. Traditional methods of lithium-ion battery cathode production, once stalwarts in the field, are now deemed infeasible, having reached the limits of their potential in improving electrode properties as well as in increasing production rate. In this landscape, intensive dry mixing has emerged as a promising technology.<sup>[1,2]</sup> Unlike conventional wet processes, intensive dry mixing stands out by offering the distinct advantage of imparting favorable properties to cathode materials, such as the mechanical coating of the active material with the conductivity additive. This capability, previously elusive through other methods, sets intensive dry mixing apart. This pioneering technique is opening new avenues for enhancing the perform-

ance of batteries, aligning with the evolving requirements of contemporary energy storage applications such as increased capacity, improved safety and faster dis-/charging. Intensive dry mixing showcases its versatility by serving as both a precursor for conventional wet processes and as a key component in a completely solvent-free production method.<sup>[3,4]</sup> This dual functionality not only offers flexibility in integrating it into existing manufacturing processes but also provides a cost-effective alternative through the elimination of solvents, contributing significantly to economic viability. Moreover, intensive dry mixing has also been recently employed in construction of heteroaggregates comprising active material, conductivity additive and solid electrolyte to be used in all-solid-state batteries.<sup>[5]</sup>

Subsequently, numerous research groups have focused their resources into understanding and exploiting this innovative process. Bauer et al.<sup>[6]</sup> found that a theoretically favourable distribution of the conductivity additive could be achieved in a dry mixing process by mechanically coating carbon black onto lithium nickel manganese cobalt oxide (NMC) cathode particles. However, upon addition of the binder during electrode fabrication, the resulting cathodes actually showed significant loss in performance. In a bid to establish an experimental link between dry mixing and cathode performance, Bockholt et al.<sup>[7]</sup> found that the high dispersion attained through intensive mixing of the conductivity additive and the active material, lead to breakage of long range electrical contacts in the cathode microstructure and hence significantly increased the blend resistance. Furthermore, they were able to observe significant change in packing density related to the mixing intensity. In a

[a] A. Chauhan, C. Lischka, H. Nirschl  
Institute of Mechanical Process Engineering and Mechanics  
Karlsruhe Institute of Technology  
Kaiserstrasse 12, 76131 Karlsruhe, Germany  
E-mail: anshuman.chauhan@kit.edu

 Supporting information for this article is available on the WWW under <https://doi.org/10.1002/batt.202400051>

 © 2024 The Authors. Batteries & Supercaps published by Wiley-VCH GmbH. This is an open access article under the terms of the Creative Commons Attribution License, which permits use, distribution and reproduction in any medium, provided the original work is properly cited.

following study,<sup>[8]</sup> they found that parameter variation in the dry mixing process could be used to precisely control bulk properties like packing density and resistance of cathode blends. It was found that although electrical contacts in the blend were destroyed upon intensive mixing they could be re-established upon calendaring. In addition, the conductive additive coating on the active material surface was found to improve its cycling stability. In concurrence, Gyulai et al.<sup>[9]</sup> showed that during dry electrode manufacturing, increased intensity lead to increased homogeneity of the cathode constituents. However, this did not directly translate into cathode performance as highly homogenized cathode did not exhibit electrical connections necessary to ensure sufficient electrical conduction along the thickness of the cathode, evident through increased over-potentials observed in cyclic voltammerty measurements. Additionally, they also noted an enhancement in cyclability associated with increased homogeneity. The relation between cyclability and coating was confirmed by other groups like Chen et al.<sup>[10]</sup> and Li et al.,<sup>[11]</sup> to name a few and has been exploited further with a variety of coating substances.<sup>[12–14]</sup> In these studies, the observed change in cyclability is attributed to the hindrance of side reactions at the cathode-electrolyte interface specially for highly reactive nickel rich active materials. Further, An improvement in electrical as well as ionic conductivity was also argued as cause of capacity retention in case of other materials like lithium iron phosphate (LFP). On the contrary, enough evidence can be found in literature<sup>[15–17]</sup> that at a certain threshold of thickness or mass fraction of the coating substance, its presence could impede the de-/intercalation reactions taking place at the cathode surface, leading to capacity loss. Thus, it is consensually accepted in contemporary literature, that intensive dry mixing leads to homogeneous mixing of cathode components and that mechanical coating of the conductivity additive leads to improvement in cyclability but could lead to capacity loss at a certain threshold. However, there seem to be discrepancies in findings relating to how the properties of dry cathode blends translate into electrochemical performance of half-cells. Moreover, since the blends investigated in the studies mentioned above were inevitably calendared to be fabricated into electrodes, the causality between microstructure obtained after mixing and the resulting performance is unclear.

In this study we establish a link between the bulk density of the cathode blends at two different intensities of dry mixing process and the electrochemical performance of their corresponding half-cells with the help of numerical evaluations. Our evaluations are based on the assumption of a solvent free manufacturing process. Herein, the downstream processes before the coating of the blend onto the current collector are absent and only the mixing step has an influence on the microstructure of the cathode. In our previous publication,<sup>[18]</sup> we showed that the comminution process of carbon black during intensive dry mixing with the active material could be characterized by the bulk density of the blend. The bulk density on the other hand was shown to influence the powder conductivity and the intensity of mixing was identified as the parameter leading to differences at similar level of deagglomer-

ation in the dry blends. Furthermore, we developed a coarse-grained discrete element method (DEM), to numerically generate particle powder structures capable of emulating the course of deagglomeration in carbon black active material blends relying on bulk density measurements acquired during the mixing process in a high intensity dry mixer. Building upon this work, particle structures representing three stages of deagglomeration at bulk density of  $957 \text{ kg m}^{-3}$ ,  $1300 \text{ kg m}^{-3}$  and  $1560 \text{ kg m}^{-3}$  were transformed into half-cell cathode geometries based on a previously developed numerical scheme.<sup>[19]</sup> The measured powder conductivity at two different intensities represented by the mixing tool speeds,  $20 \text{ ms}^{-1}$  and  $25 \text{ ms}^{-1}$ , was employed to capture changes in the electrical properties. Furthermore, a coating factor based on the increment in conductivity at a given bulk density was implemented to account for the inhibition of the intercalation reaction at the cathode-electrolyte material surface. It was assumed that the impact of coating of the conductivity additive was well represented by the increased electrical conductivity and dampened intercalation and no significant change in the ionic conduction at the active material surface needed to be accounted for. This assumption is justified for nickel rich active materials like NMC as the electrical conductivity of such materials is much greater than their ionic conductivity<sup>[20]</sup> such that a coating of the active material with conductivity additive does not lead to significant improvement in the distribution of incident lithium ions over the surface of the material, rather the presence of the passive material at the cathode-electrolyte interface is expected to dampen the intercalation reaction. Such would not be the case in case of materials with significantly low electrical conductivity like LFP.<sup>[21]</sup> The half-cell geometries with the assigned properties, hence formed the basis for the following numerical evaluations. At first, a structural characterization was carried out wherein the tortuosity and specific active surface area were reported similar to our preceding publication, followed by the numerical determination of the effective electrical conductivity of the variants. Finally, scale resolving electrochemical simulations representing galvanostatic discharge at a low (0.5 C) and high current (5 C) were carried out to evaluate performance at contrasting operating conditions (high energy/high power). However, due to the exclusive use of single discharge simulations, estimations regarding cyclability were not conducted. Additionally, since the electrochemical model lacks a degradation component, the evaluation of such aspects was considered beyond the scope of this study.

## 2. Numerical Method

### 2.1. Idealized Microstructure Generation

The generation of computational half-cell domains for the purpose to this study was undertaken in two stages. At first, idealized particulate structures, capable of imitating change in bulk density with change in the state of deagglomeration of the conductivity additive in dry cathode blends, were assembled

using coarse graining in a DEM model. This model was previously calibrated<sup>[22]</sup> for lithium-ion battery materials. Owing to the extremely small size of carbon black particles,<sup>[23,24]</sup> it is computationally infeasible to account for all the conductivity additive particles needed for the construction of a cathode of realistic thickness in DEM simulations. Hence, the particulate structures assembled in this stage exhibit a coarse graining factor of approximately 200 and comprise two components: the active material in form of NMC 622 and carbon black as the conductivity additive present in mass fraction ratio of 98:2 wt%. The active material particles are modelled as smooth spheres (red) and the carbon black agglomerates (black) constructed as fractal structures with the help of a previously developed algorithm<sup>[25]</sup> in accordance with the tunable dimension method as shown in Figure 1. The fractal dimension  $d_f$  is set to 2.5 and with variation in the primary particle number  $n_p$ , different stage of comminution could be represented. Consequently, the number of primary particles comprising the carbon black agglomerates were chosen as the basis of nomenclature for the investigated variants CB1000, CB35 and CB1, in the order of increasing bulk density. In order to numerically obtain these structures a blend of active material and carbon black (representing different stages of deagglomeration) was filled in a simulation box with the dimensions 22×22×22 mm, following the evaluation of the attained bulk

density and ultimately compacted with the same pressure as in the case of powder conductivity measurements.<sup>[18]</sup> Since the volume of the simulation box is constant, the mass of the dry blends filled in varies with the bulk density such that the most dense powders leads to the box being filled with the most number of particles as tabulated in Table 1.

In the second stage, the particulate geometries were transformed into idealized half-cell computational domains. Since, solvent free manufacturing processes are usually associated with very low binder content,<sup>[26]</sup> it can be reasonably inferred that the presence of the binder in such cases, does not exert a noteworthy influence on the cathode performance. Consequently, no compelling requirement to explicitly account for the binder in the performance evaluation of half-cells was assumed. Furthermore, the investigations were restricted to uncalendered cathodes. To transform the particulate structures into computational domains representative of real cathodes the particulate structures were extended periodically.<sup>[19]</sup> This ensures that the numerical result obtained for the investigated domain can be transmitted to the scale of the entire cathode. In addition, the coarse grained particulate assemblies were scaled back to the microscale, since the electrochemical simulation at the coarse grain scale were infeasible. The final half-cell domain hence constructed, has the dimension 110×110  $\mu\text{m}$  in the plane and the height of the individual cathode attained after

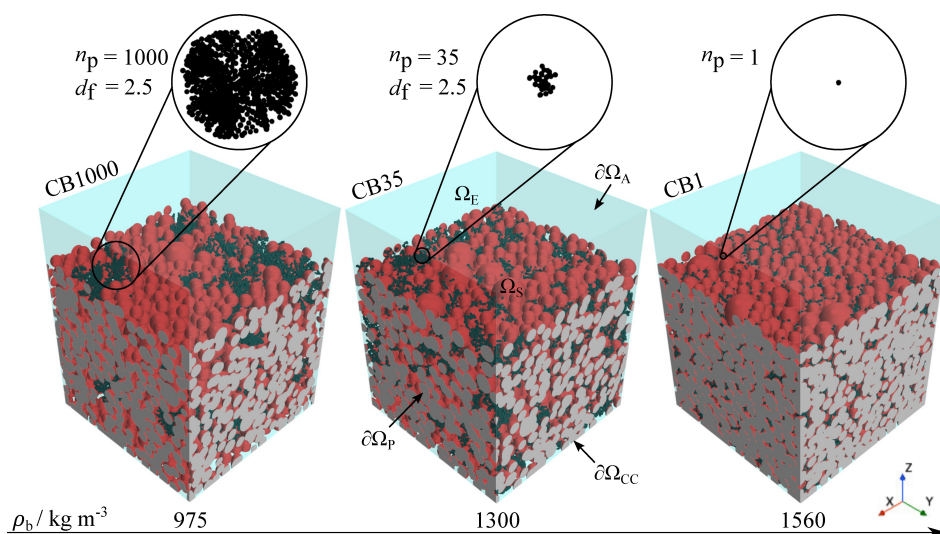


**Figure 1.** Idealized half-cell computational domains investigated in this contribution. The variants are arranged in the ascending order of bulk density  $\rho_b$ , from left to right. The areas marked with circles are zoomed into, to show the carbon black agglomerate structure at a given bulk density. The middle variant has been labeled to exhibit the regions and boundaries of the half-cell. The red and black spheres comprise the solid region and the electrolyte region is present in the pores of the solid and above it shown in blue. The anode and cathode current collector are the top (in the electrolyte region) and bottom (in the cathode region) of the half cell respectively and the cross-sections in grey are the periodic boundaries of the half-cell.

**Table 1.** Structural properties of the coarse-grained half-cell computational domains.

Bulk Density/ $\text{kg m}^{-3}$	Total Particles/-	Porosity/ $\%^{[18]}$	Tortuosity/ $^{-[18]}$	Cathode Height/ $\mu\text{m}$	Cathode Volume/ $\mu\text{m}^3$	Total Sp. Surface Area/ $\mu\text{m}^{-1}$
975	31639	60	1.33	105.33	502501	0.73
1300	35059	57	1.35	103.57	539254	0.71
1560	52136	29	2.41	102.64	878083	0.50

compression in the first step is dependent on the bulk density of the blend. It consists of two non-overlapping, closed, finite volume element domains namely the solid region, cathode  $\Omega_S$  and the fluid region, electrolyte  $\Omega_E$  as shown in Figure 1. The cathode regions is further subdivided in the active domain  $\Omega_S^{AM}$  and the passive domain  $\Omega_S^{CBD}$  based on the position of the respective particles and the electrolyte region contains the separator  $\Omega_E^{SEP}$ , seen as void region above the cathode in the figure, as its subdomain. It is evident from the figure that with increasing degree of deagglomeration and rising bulk density the dispersion of carbon back in the system increases. However, despite the increased dispersion at higher bulk density, the increased mass with the total particles, results in decrease in the volume specific total surface area as denoted in Table 1 along with other properties. Moreover, the accompanying reduction in porosity with denser bulks, leads to an increase in the tortuosity as can be read from the table.

## 2.2. Characterization

In our precursor publication,<sup>[18]</sup> we carried out the characterization of the coarse-grained half-cell geometries discussed in the previous Section 2.1. In this section, a numerical method for the characterization of the half-cell computational domains scaled back to the microscale, has been elaborated. Since the porosity and the tortuosity are not expected to change in the scaling process, these were adopted as half-cell characteristics on the microscale. In our previous work, literature values were employed for the conductivities of individual cathode components. However, in this study, for the determination of the effective electrical conductivity of the half-cell computational domains, powder conductivities of bulks measured by Lischka et al.<sup>[18]</sup> at changing bulk densities and intensities (indicated by tool speed) were incorporated as spatially constant electrode conductivity  $\kappa_S$  into the numerical method developed by Kespe et al.<sup>[27]</sup> Due to the complexity of measuring or numerically evaluating the individual conductivity of constituent materials and their contact resistance, the previously measured powder conductivity was adopted as the initial estimate for the intrinsic conductivity of the bulks. The set of equations utilized for the evaluation have been denoted in Table 2. In order to obtain the effective value of conductivity for the half-cell  $\kappa_S^{eff}$  using the Relation 2.4, an electrical flux  $\vec{i}$  was induced in the solid domain  $\Omega_S$  over the cross section  $\Delta x \times \Delta y$  (lateral dimensions) via a gradient over the thickness  $H$  of the cathode, such that the

Table 2. Model equations for determination of effective electrical conductivity.	
$\Omega = \Omega_S, \partial\Omega = \partial\Omega_{CC} \cup \partial\Omega_{SE} \cup \partial\Omega_P \cup \partial\Omega_T$	
$\nabla \cdot (\kappa_S \cdot \nabla \phi) = 0$	(2.1)
$\nabla \phi \cdot \vec{n} = 0$ on $\partial\Omega_{SE}$	(2.2)
$\vec{i} = \kappa_S \cdot \nabla \phi$	(2.3)
$\kappa_S^{eff} = \frac{\int_{\partial\Omega_{CC}} \vec{i} \cdot \vec{n} \cdot H}{(\phi_T - \phi_{CC}) \cdot \Delta x \cdot \Delta y}$	(2.4)

potential at the top surface  $\partial\Omega_T$  was set to  $\phi_T$  and at the bottom surface  $\partial\Omega_{CC}$  contacting the current collector to  $\phi_{CC}$ . Since the conduction of the electrical current take place exclusively in the solid region of the half cell, the boundary condition 2.2 on the cathode-electrolyte interface  $\partial\Omega_{SE}$  was implemented. Besides, periodic boundary conditions were implemented at the lateral extremities  $\partial\Omega_P$ . Upon solving for conservation of charge Equation 2.1 with the given boundary conditions in a finite volume method based solver in Open FOAM, Version 10, the potential in the entire region was resolved and hence, with the integral of the charge flux  $\int \vec{i} \cdot \vec{n} \cdot \partial\Omega_{CC}$  at the current collector, the effective conductivity was calculated. The methodology used to compute the tortuosity in the previous section is very similar and has been discussed in detail previously.<sup>[28]</sup> In a further effort to comprehend the electrical connections established in the half-cell, an analysis of the contacts formed at various stages of comminution was conducted using a self written MATLAB<sup>[29]</sup> script. Given the current inability to accurately describe and validate the contact area formed, along with the resulting contact resistance during deagglomeration in a dry mixer using the present DEM model, all contacts identified in the system were treated as similar i.e., presented an equivalent resistance to current flow. The objective of the analysis, therefore, was not to quantify the electrical resistance in the half-cell but rather to provide a means of assessing the development of new pathways and their deterioration during the course of dry mixing. An important evaluation arising from such an analysis is the characterization of the increased interaction between the active material and the conductivity additive through the alteration in the accessible active surface area. Given that the primary carbon black particles are deemed impermeable to ionic flow, the contact formation between carbon particles and the active material particle results in the unavailability of the area previously accessible for the intercalation reaction. Consequently, the surface area available for intercalation can be stated as:

$$S_V = \frac{\text{Total Active Surface Area} - \text{Active Surface Area occupied by the CBD}}{\text{Cathode Volume}} \quad (1)$$

## 2.3. Performance Evaluation

The investigation presented in this study leverages the spatially resolved 3D microstructural model initially proposed by Kespe et al.<sup>[30]</sup> for evaluating the performance of a half-cell. This model employs mass and charge balance equations to depict the transport of lithium ions and electrons within the half-cell, with the generalized forms of these balances expressed as Eq. (2) and (3). In these equations,  $c$  denotes concentration,  $t$  represents time,  $\vec{n}$  signifies mass flux, and  $\vec{i}$  denotes current flux.

$$\frac{\partial c}{\partial t} = -\nabla \cdot \vec{n} \quad (2)$$

$$\nabla \cdot \vec{i} = 0 \quad (3)$$

In the solid region of the half-cell, the mass flux  $\vec{n}_s$ , is represented as the gradient of solid concentration  $c_s$ , by Eq. (3.1) and the charge flux  $\vec{i}_s$ , as the gradient of solid potential  $\phi_s$ , by Eq. (3.3) as shown on the left column of Table 3. The diffusion in the active subdomain  $\Omega_s^{AM}$  and the passive subdomain  $\Omega_s^{CBD}$ , has been modelled to restrict solid state lithium diffusion to the former such that, the diffusion coefficients of the respective subdomains follow,  $D_s^{CBD} \rightarrow D_s^{AM}$ . Within the scope of this investigation, the electrical conductivity  $\kappa_s$  of the entire solid domain on the other hand was set to a spatially constant value derived from measurements as mentioned in Section 2.2. Concurrently, for the electrolyte domain  $\Omega_e$ , mass flux  $\vec{n}_e$  and the charge flux  $\vec{i}_e$  has been formulated as Eq. (3.2) and (3.4) respectively, as shown on the right column of the table. These relations are derived from the theory of concentrated solutions such that  $c_e$  refers to electrolyte concentration,  $\phi_e$  to the electrolyte potential and  $t_+^0$  to the transference number. The universal constants  $F$  and  $R$  represent Faraday's constant and Gas constant respectively. Under the assumption of isothermal operational conditions the temperature  $T$ , is set to 298 K. Upon plugging these into Eq. (2) and (3), it is evident that the balance equation are coupled. This is not the case for the solid region, owing to the separation of charge and mass transfer in the solid region of the half-cell. Furthermore, in case of the electrolyte domain the concentration dependence of the electrolyte conductivity  $\kappa_e$  (Eq. (4)) and the diffusivity  $D_e$  (Eq. (5)), is modelled with the help of polynomial expressions extracted from the parameterization carried out by Less et al.<sup>[31]</sup> for completely dissociated lithium hexafluorophosphate (LiPF<sub>6</sub>) in a mixture of ethylene carbonate and ethyl methyl carbonate.

$$\kappa_e = -2.39 \cdot 10^{-11} \cdot c_e^4 + 1.21 \cdot 10^{-7} \cdot c_e^3 - 2.89 \cdot 10^{-4} \cdot c_e^2 + 0.32 \cdot c_e - 2.789 \quad (4)$$

$$D_e = 1.2 \cdot 10^{-21} \cdot c_e^4 - 6.5 \cdot 10^{-18} \cdot c_e^3 + 1.14 \cdot 10^{-14} \cdot c_e^2 - 8.06 \cdot 10^{-12} \cdot c_e + 2.24 \cdot 10^{-9} \quad (5)$$

At equilibrium conditions, no net transfer of charger or mass takes place at the interface of the solid and electrolyte region such that the over-potential  $\eta$  defined by Eq. (6) is zero. Herein, the equilibrium potential  $U_{eq}$  is defined in relation to the solid concentration by Eq. (7).<sup>[32]</sup>

$$\eta = \phi_s - \phi_e - U_{eq} \quad (6)$$

$$U_{eq} = 13.4905 - 10.96038 \cdot c_s + 8.203617 \cdot c_s^{1.358699} - 3.10758 \cdot 10^{-6} \cdot e^{(127.1216 \cdot c_s - 114.2593)} - 7.033556 \cdot c_s^{-0.03362749} \quad (7)$$

However, when the half-cell is operated in a manner such that the galvanostatic potential is not equal to the equilibrium potential, such that  $\eta \neq 0$ , a net current is initiated. The net current associated with change in the over-potential is modelled with the help of a Butler-Volmer type relation which dictates the kinetics of the intercalation reaction at the cathode-electrolyte interface by means of the intercalation current density  $i_{BV}^-$ .<sup>[33]</sup> Under the assumption of symmetry such that the cathodic apparent transfer coefficient  $\alpha_c$  is equal to the anodic apparent transfer coefficient  $\alpha_a$ , the relation is given by Eq. (8). The expression is split at the active  $\Omega_{s,e}^{AM}$  and passive  $\Omega_{s,e}^{CBD}$  parts of the cathode-electrolyte boundary  $\partial\Omega_{s,e}$ . At the passive boundary the current is set to zero to ensure inactivity of the conductivity additive, carbon black. While at the active boundary, the current is proportional on the solid concentration, the residual solid concentration, electrolyte concentration and the proportionality constant  $k'_{BV}$ .

$$i_{BV}^- = \begin{cases} 2 \cdot k'_{BV} (c_s^{\max} - c_s)^\alpha (c_e)^\alpha \sinh\left(\frac{F}{2RT} \eta\right) & \text{on } \partial\Omega_{s,e}^{AM} \\ 0 & \text{on } \partial\Omega_{s,e}^{CBD} \end{cases} \quad (8)$$

The proportionality constant is further composed of a Butler-Volmer reaction rate constant, referred to as the exchange coefficient<sup>[34]</sup> or exchange current density factor<sup>[32]</sup> in literature and a coating factor  $f_c$ . The former is a material specific fitting parameter determined by the fit between the current density and the intercalated lithium measurements.<sup>[35]</sup> The coating factor  $f_c$ , on the other hand is dependent on the intensity of mixing and has been used to model the adverse effects of coating during intensive mixing. It is assumed that the fractional change in the powder conductivity at a given bulk density upon change in intensity of the mixing tool (as depicted in the results section), arises only due to the influence of coating. Hence, the Butler-Volmer reaction rate constant was scaled down with the same fraction, to model the consequence of this change on the intercalation phenomenon as indicated by Eq. (9). Here,  $f_c^{pb,i}$  represents the coating factor and  $\kappa_{pow}^{pb,i}$  the electrical conductivity at a given bulk density  $\rho_b$  and intensity  $i$  as shown in Figure 2a.

$$f_c^{pb,i} = \frac{\kappa_{pow}^{pb,i}}{\kappa_{pow}^{pb,i-1}} \quad (9)$$

**Table 3.** Mass and current flux in cathode and electrolyte domain.

$\Omega_s = \Omega_s^{AM} \cup \Omega_s^{CBD}$ , $\partial\Omega_s = \partial\Omega_{s,e} \cup \partial\Omega_{cc} \cup \partial\Omega_{p,s}$	$\Omega_e = \Omega_e^{REST} \cup \Omega_e^{SEP}$ , $\partial\Omega_e = \partial\Omega_{s,e} \cup \partial\Omega_A \cup \partial\Omega_{p,e}$
$\vec{n}_s = -D_s(\vec{x}) - \nabla c_s$ (3.1)	$\vec{n}_e = -D_e \cdot \nabla c_e + \frac{t_+^0}{F} \cdot \vec{i}_e$ (3.2)
$\vec{i}_s = \kappa_s \cdot \nabla \phi_s$ (3.3)	$\vec{i}_e = -\kappa_e \cdot \nabla \phi_e + \frac{2RT\kappa_e}{F} (1 - t_+^0) \nabla \ln c_e$ (3.4)

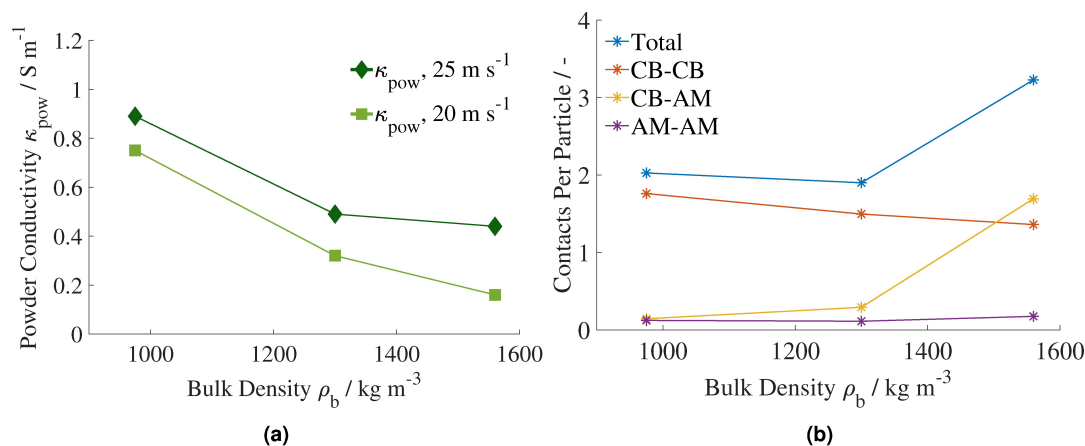


**Figure 2.** Structural characteristics of the half-cells. a) Measured powder conductivity.<sup>[18]</sup> b) Types of contact per particle relative to total particles in half-cell computational domain.

Thus, as an initial estimate of the effect of coating, it is assumed that the intercalation reaction rate scales linearly and inversely with coating. The least coated state i.e. the smallest bulk density at the lowest tool speed is set as the reference. It is further assumed that at the lower tool speed no significant change in the coating condition takes place and hence the scaling factor is always unity. The scaling factors  $f_C^{\text{pb},j}$  as well as the proportionality constants  $k_{\text{BV}}^{\text{pb},j}$  thus calculated, have been denoted in Table 4.

At the lateral extremities  $\partial\Omega_p$  of the solid as well as the electrolyte domains periodic boundaries are implemented such that material and charge transfer takes place across the end faces that lie opposite to each other. The bottom surface of the solid domain  $\partial\Omega_{\text{CC}}$  is modelled as a perfectly conducting current collector subjected to galvanostatic operational conditions and the top surface  $\partial\Omega_A$  is considered to be composed of metallic lithium that serves as an ideal and endless supply of lithium. To ensure neutrality of charge in the half-cell Eq. (10) was implemented. This ensures that at all times the charge initiated at the anodic surface is consumed at the surface of the solid region in the half-cell. The entire set of boundary conditions and model equations are implemented in the open source platform OpenFOAM, Version 10. A list of all additional model parameters has been summarized in Table 5 for the sake of completeness.

$$\vec{i}_{\text{BV}} \cdot \vec{n}_S = \vec{i}_E \cdot \vec{n}_E \quad (10)$$

In order to derive a quantitative measure of the performance of the half-cell from the scale resolving simulations, the potential of the half-cell as recorded at the current collector is

plotted against the depth-of-discharge (DOD). The DOD, is a measure of the exhausted capacity of the half-cell during galvanostatic discharge w.r.t to maximum theoretical capacity and is dependent on the maximum  $c_{S,\text{max}}$  initial  $c_{S,\text{ref}}$  and current  $c_s(\vec{x}, t)$  lithium concentration as state in Eq. (11).

$$\text{DOD} = \frac{\int (c_s(\vec{x}, t) - c_{S,\text{ref}})}{\int (c_{S,\text{max}} - c_{S,\text{ref}})} \quad (11)$$

$$\text{UC} = \frac{\text{DOD}(\text{COV})}{\text{DOD}_{\text{eq}}(\text{COV})} \cdot 100 \quad (12)$$

The simplest measure of performance that can be extracted from the DOD, is the utilizable capacity (UC) which is the ratio of the capacity exhausted under given operational condition to the theoretical capacity exhaustion possible under equilibrium conditions until a certain predefined cut-off voltage (COV) as stated in Eq. (12). The chosen operational conditions for the evaluations in this work represent the spectrum of operational condition to which modern lithium-ion batteries are subjected. The C-Rate of 0.5 C represents the bottom half of the spectrum, found to have its application usually in high-energy cells. While, 2 C commonly applied to high power cells covers the other end. Since the absolute current following through the current collector at a given C-Rate and the theoretical capacity are both a function of the amount of active material ( $V_s$ ) as stated by Eq. (13),<sup>[36]</sup> UC cannot be used to compare the variants under consideration.

**Table 4.** Coating factor as a function of bulk density and mixing tool speed.

Bulk Density/ $\text{kg m}^{-3}$	$f_C^{\text{pb},25} / -$	$k_{\text{BV}}^{\text{pb},25} / \text{A m}^{2.5} \text{mol}^{-1.5}$	$f_C^{\text{pb},20} / -$	$k_{\text{BV}}^{\text{pb},20} / \text{A m}^{2.5} \text{mol}^{-1.5}$
975	1.18	$1.24 \cdot 10^{-6}$	1	$1.4693 \cdot 10^{-6}$
1300	1.53	$9.6 \cdot 10^{-7}$	1	$1.4693 \cdot 10^{-6}$
1560	2.75	$5.24 \cdot 10^{-7}$	1	$1.4693 \cdot 10^{-6}$

Table 5. Parameters for the spatially resolved electrochemical model on the microscale.			
	Value	Unit	Ref.
<b>Cathode</b>			
Active Material Coefficient of Diffusion $D_s^{\text{AM}}$	$4.3032 \cdot 10^{-14}$	$\text{m}^2 \text{s}^{-1}$	[32]
CBD Coefficient of Diffusion $D_s^{\text{CBD}}$	$1 \cdot 10^{-20}$	$\text{m}^2 \text{s}^{-1}$	[36]
Initial Cathode Potential $\phi_{s,\text{ref}}$	4.3	V	[38]
Active Material Initial Lithium Concentration $c_{s,\text{ref}}^{\text{AM}}$	18409.57	$\text{mol m}^{-3}$	[32]
Active Material Maximum Lithium Concentration $c_{s,\text{max}}^{\text{AM}}$	50451	$\text{mol m}^{-3}$	[32]
CBD Lithium Concentration $c_{s,\text{ref}}^{\text{CBD}}$	0	$\text{mol m}^{-3}$	[36]
<b>Electrolyte</b>			
Initial Electrolyte Potential at Anode Surface $\phi_{E,\text{ref}}$	0	V	[38]
Transfer Number $\epsilon_+^0$	0.4	–	[31]
Initial Lithium Concentration $c_{E,\text{ref}}$	1000	$\text{mol m}^{-3}$	[36]
<b>Separator</b>			
Porosity $\epsilon_{\text{SEP}}$	0.5	–	[36]
Tortuosity $\tau_{\text{SEP}}$	1.5	–	[36]
<b>Butler-Volmer Kinetics</b>			
Butler-Volmer Reaction Rate Constant $k_{\text{BV}}$	$1.4693 \cdot 10^{-6}$	$\text{A m}^{2.5} \text{mol}^{-1.5}$	[32]
Cathodic Apparent Transfer Coefficient $\alpha_c$	0.5	–	[32]
Anodic Apparent Transfer Coefficient $\alpha_a$	0.5	–	[32]

$$I_{\text{CC}}^{\text{Theo}} = C \cdot \frac{F}{3600} \cdot \int_{\Omega_s} (c_{s,\text{max}} - c_{s,\text{ref}}) dV_s \quad (13)$$

Thus an approach similar to the one followed by Cernak et al.<sup>[37]</sup> using gravimetrically and volumetrically normalized performance determinants, utilizable energy density (UED) and utilizable power density (UPD) was employed. Following Eq. (14), the utilizable energy in the half-cell was calculated in watt seconds (Ws) using the time dependent potential  $\phi_{s,\text{CC}}(t)$  in volt (V) and the galvanostatic current  $I_{\text{CC}}(t)$  in ampere (A) at the cathode current collector. The limits of the integral were set from the start of discharge  $t(0)$  to the point in time in seconds  $t(\text{COV})$  when the COV is reached. In cases where the COV could not be reached till the end of the discharge or the highest achievable DOD was limited due to transport limitations, the latest time recorded was set as the upper limit.

$$\text{UE} = \int_{t(0)}^{t(\text{COV})} \phi_{s,\text{CC}}(t) \cdot I_{\text{CC}}(t) dt \quad (14)$$

Upon dividing the UE with the mass of the investigated half cell the gravimetric utilizable energy density was calculated as Eq. (15). Here,  $V_s$  represents the cathode volume and  $\rho_s$  the density of the cathode calculated based on the method applied by Hein et al.<sup>[38]</sup> Wherein,  $w_i$  represents the mass fraction of the constituent particle type and  $\rho_i$  its density. For this evaluation,

the density of NMC 622 was set to  $4780 \text{ kg m}^{-3}$  and density of carbon black to  $1850 \text{ kg m}^{-3}$ . In addition, the factor 3600 is used to convert the final unit to watt hour per kg ( $\text{Wh kg}^{-1}$ ).

$$\text{UED}_G = \frac{\text{UE}}{\rho_s \cdot V_s \cdot 3600} \quad (15)$$

$$\rho_s = \frac{1}{\sum_i \frac{w_i}{\rho_i}} \quad (16)$$

Similarly, upon dividing the UE by the volume of the scaled simulation box  $V_{\text{box}}$  ( $110 \times 110 \times 110 \mu\text{m}$ ), in which the particles were initially filled the volumetric utilizable energy density of the half cells can be calculated using Eq. (17), in watt hour per cubic meter ( $\text{Wh m}^{-3}$ ).

$$\text{UED}_V = \frac{\text{UE}}{V_{\text{box}} \cdot 3600} \quad (17)$$

Finally in order to determine the respective gravimetric and volumetric utilizable power density, the previously determined energy density is divided by the discharge time resulting in the power density evaluation in watt per kg ( $\text{W kg}^{-1}$ ) and watt per cubic meter ( $\text{W m}^{-3}$ ) respectively.

$$\text{UPD}_{G/V} = \frac{\text{UED}_{G/V} \cdot 3600}{t(\text{COV}) - t(0)} \quad (18)$$

### 3. Results and Discussion

#### 3.1. Characterization

In Figure 2, the structural characteristics of the half-cell have been depicted. The value of the powder conductivities plotted in the Figure 2a were used as a measure of the intrinsic conductivities of the cathode component blend in the half-cell as mentioned in Section 2.2. The deterioration of powder conductivity with increasing bulk density due to the breakage of electrical contacts on intensive mixing has been elaborated in our previous publication.<sup>[18]</sup> Since, the bulk density has been used in this study to reflect the deagglomeration process, it is assumed that the microstructure attained during mixing at a given bulk density and hence degree of deagglomeration, remains the same irrespective of the intensity. However, it is observed that the powder conductivity in the bulk rises as the tool speed increases. This is attributed to the enhanced coating of the conductivity additive on the active material through intensive mixing, as evidenced by the notable increase in powder conductivity depicted in the figure as intensity increases. Given that the coating phenomenon is anticipated to be linked with minor proportions of the conductivity additive, it is presumed to have an insignificant impact on both the bulk density and the arrangement of constituents in the microstructure. Thus, the microstructure attained at a given bulk density is fixed and can be described by the analysis of its contacts as shown in Figure 2b.

Since the mass of the variants and hence the number of particle of the variants investigated in this study is different, the evaluated contacts were normalized using the total number of particles in the respective variant to ensure comparability. In Figure 2b, "Total" represents the sum of all contacts, "CB-CB" represents the contacts within carbon black agglomerates as well as the inter-agglomerate contacts formed with other carbon black agglomerates. "CB-AM" represents the contacts

between carbon black and active material particles and "AM-AM" the inter-active-material particle contacts. It can be seen from the figure, that with increasing bulk density the total contacts per particle decrease very slightly until  $\rho_b \leq 1300 \text{ kg m}^{-3}$  in the direction of increasing bulk density. Looking at the composition of the total contacts in the figure it is evident that, up till this point the lost CB-CB contacts due to the fragmentation of the carbon black agglomerates overweigh the newly formed CB-AM contacts. However, at higher degree of deagglomeration  $> 1300 \text{ kg m}^{-3}$  a sharp increase in the Total contacts is observed. This is caused on the one hand, by the increasing fragments of carbon black agglomerates that establish new contacts with nearby active material particles thus increasing the CB-AM contacts and on the other hand by the increased homogenisation at higher degree of deagglomeration, that decreases the inter carbon black agglomerate contacts hence reducing the CB-CB contacts further. The AM-AM contacts remain constant as expected, as no fractioning of the active material takes place.

The progression of the contacts with the changing bulk density can be used to explain trends seen in the characteristics of the half-cell variants plotted in Figure 3. An increase in the CB-AM contact per particle with bulk density, as observed from the analysis of contacts means that more of the active material particle surface area gets occupied by the newly formed contacts, this in turn leads to decrease in the percentage of the volume specific total surface area available for intercalation as seen in Figure 3a. Proportional to trend in the CB-AM contacts the active surface decreases slightly at first, followed by a sharp decline at the highest bulk density variant (CB1). Similarly, The trend in the effective electrical conductivity (Figure 3b, right axis) can be explained by an interplay between the decreasing intrinsic conductivity of the bulk (Figure 2a) at a given intensity and the trend in the total number of contacts. This leads to a decrease in the effective electrical conductivity with increasing bulk density until  $\rho_b \leq 1300 \text{ kg m}^{-3}$ . However beyond this threshold,  $\kappa_{\text{eff}}$  increases due to the sharp increase in total contacts despite the decreasing intrinsic conductivity. The offset in the effective conductivity curves over changing tool speed (changing intensity) is similar to the offset in the powder

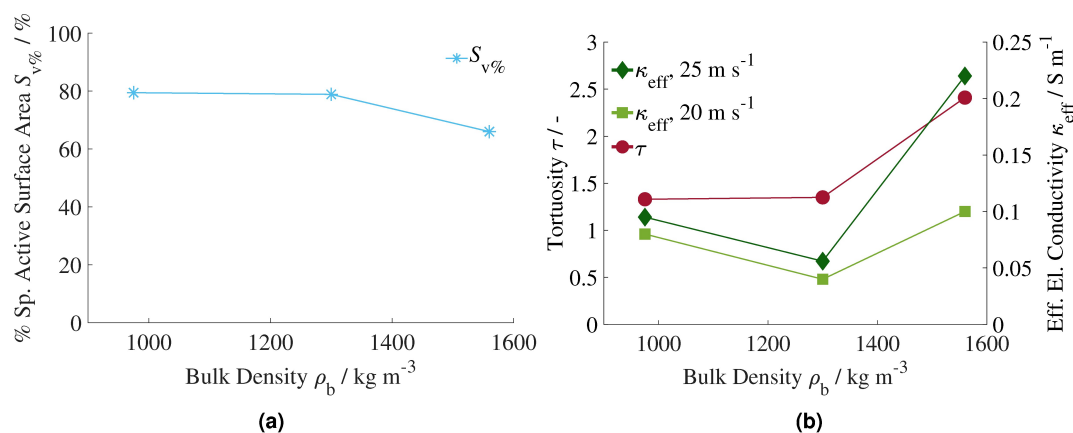


**Figure 3.** Characterization of the half-cells. a) Specific active surface area as a percentage of the total volume specific surface area. b) Tortuosity (left axis) and effective electrical conductivity (right axis) at changing tool speeds.



conductivity (Figure 2a), attributed to the coating phenomenon as mentioned earlier. Finally, the decreasing porosity as denoted in Table 1, accompanied by an increase in the total number of contacts per particle explains the trends in tortuosity as seen in Figure 3b on the left axis. Since the structure of the variant remains the same with changing intensity, only one set of curves are shown for the active surface area and tortuosity and contacts unlike the conductivities.

### 3.2. Performance Evaluation: Half-Cell Potential

In order to quantify the impact of the evaluated characteristics of the variants on their performance, scale resolving electrochemical simulations were carried out. The half-cell potentials at the current collector obtained from the resolved solution of the model equations mentioned in Section 2.3, as plotted in Figure 4, serve as the first estimate in this regard. The presented half-cell evaluations have been made at two different operational conditions namely, 0.5 C discharge representing the high energy application (dotted lines) and 2 C discharge representing the high power application (solid lines). Since the lower C-rate presents a state closer to the equilibrium potential, it is always associated with lower over-potential and hence higher half-cell potential. In Figure 4a, the influence of coating is disregarded. Thus, the intrinsic conductivity of the variant at a given bulk density is the only differentiating parameter. On the other hand, in Figure 4b, the influence of coating has been modelled explicitly using a coating factor  $f_c$ , as mentioned in Section 2.3 and the tool speed in this case has been demarcated with an asterisk symbol (\*). The values of the coating factor implemented at respective bulk density and intensities can be read from Table 4. Since, no physical quantification of the coating phenomenon could be carried out within the scope of this work, for all upcoming evaluations both cases would be considered to ensure objectivity.

In Figure 4, each sub-figure depicts half-cell potential curves distinguished by unique colors corresponding to different bulk densities. Additionally, within each color, varying shades denote different intensities, with darker tones indicating higher inten-

sity (tool speed  $25 \text{ ms}^{-1}$ ) and lighter tones signifying lower intensity (tool speed  $20 \text{ ms}^{-1}$ ). In both the figures it is evident that, at higher bulk density and hence lower porosity in the half-cell, the potential at the current collector lies lower for the respective operational conditions over the entire depth-of-discharge irrespective of the intensity. The larger absolute current resulting from the larger volume of the denser variants in both operational conditions along with the increased intercalation current density due to reduced surface area lead to a higher over-potential, which in turn results in a lower operational voltage (see Eq. (8) and (13)). In comparison, it can be further inferred from the figures that at a given intensity the impact of changes in the effective conductivity with changing bulk density on the half-cell potential are insignificant. However, in Figure 4a the difference in potential for the variants at changing intensities but constant bulk density are indeed solely related to differences in the effective conductivities. Lower conductivity leads to a higher ohmic losses hence the half-cell potential recorded for variant with lower effective conductivity at the lower intensity ( $20 \text{ ms}^{-1}$ ) is lower. Since, the drop in potential scales with applied current the differences in the half-cell potential with changing intensity are more significant at the higher C-rate as can be seen in the figure.

In case of Figure 4b, the difference in potential observed with changing intensities but constant bulk density, are a combination of the influence of the effective conductivity and reduced Butler-Volmer reaction rate resulting from the coating factor. At the lower C-Rate (0.5 C) where the influence of the effective conductivity is negligible, the variants at lower intensities ( $20 \text{ ms}^{-1}$ ) exhibit higher half-cell potential, despite the lower effective electrical conductivity. Here, the effect of the reduced Butler-Volmer reaction rate dominates, such that a higher over-potential is needed to keep up the same intercalation current density due to the reduced proportionality factor  $k'_{BV}$  for the higher intensity at tool speed  $25 \text{ ms}^{-1}$  (see Eq. (8)). This in turn reduces the half-cell potential. A similar reduction in potential is not observed at the lower intensity because of the assumption in Section 2.3 that, no coating takes place at the lower tool speed (see Table 4). Thus, the half cell potential reported in Figures 4a and 4b is the same for tool speed

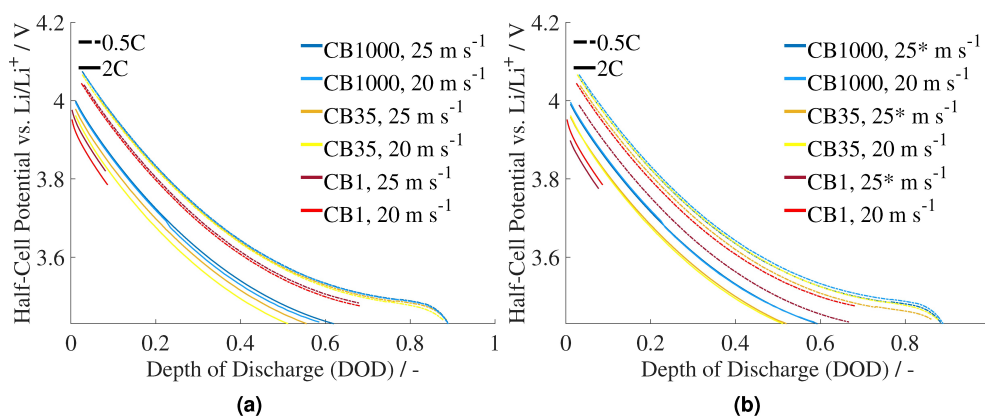


**Figure 4.** Half-cell potential at the cathode current collector. a) Coating factor not accounted for. b) Coating factor accounted for by scaling the Butler-Volmer reaction rate constant.

$20 \text{ ms}^{-1}$ . At the higher C-rate (2 C), however, where change in conductivity leads to significant change in potential as seen in Figure 4a, the decreased half-cell potential due to the reduced reaction rate is compensated by the effective conductivity such that the potential at changing intensities coincide in all cases except at the highest bulk density, where it remains under compensated in Figure 4b. An analysis of the half-cell potentials alone gives the impression that the variant at the lowest bulk density (CB1000) performs the best under all operation conditions. However, as would be shown with the help of following results this inference does not always stand.

### 3.3. Performance Evaluation: Lithium Concentration Distribution

Another indication of performance of half-cell variants can be derived from analysis of the lithium concentration distribution. Such an analysis reveals further insights into the transport mechanisms of the half-cell. In Figure 5, the relative lithium concentration on the half cell variants at tool speed  $25 \text{ ms}^{-1}$  without consideration of the coating factor have been displayed at an instance close to the end of a 0.5 C discharge. Since, the effective electrical conductivity does not play a significant role at lower currents and the influence of the coating factor is spatially constant, the lithium distribution in the variants at the higher intensities and no coating have been discussed in detail, in an exemplary manner to highlight the ionic conduction limitations. In the figure, the active material particles exhibit significantly higher lithium concentration than the carbon black particles. This is because the active material particles gain lithium concentration upon lithiation during discharge, whereas the carbon black particles are inert and remain at the initial concentration  $0 \text{ mol m}^{-3}$  (Table 5). Moreover, it is evident that the smaller active material particle tend to accumulate lithium faster owing to their higher surface to volume ratio and smaller solid diffusion lengths as was observed by Ngandjong et al.,<sup>[39]</sup> for all the variants.

The spatial distribution of lithium in the half-cell is strongly dependent on the conduction phenomenon. On the one hand, sufficient ionic conduction is essential to carry the lithium ions from the anodic source to farthest end of the half cell close to the cathode current collector (see Figure 1). On the other hand, electrons are required to be carried in the opposite direction from their source at the cathode current collector to the top of the cathode near the anode. Hence, under lower current conditions (0.5 C) where electrical conduction is not the restricting factor, the CB1 variant's lower porosity, as indicated in Table 1, leads to inadequate ion conduction. Consequently, ions struggle to penetrate the cathode thickness swiftly, resulting in a preferential intercalation of lithium primarily at the top of the cathode. This phenomenon is observable in Figure 5, through an increased lithium concentration at the top of the solid region of the CB1 variant. Because of the uneven distribution of lithium ions originating at the anodic surface, the capacity of a large proportion of the CB1 variant (below the top surface) remains unutilized, unlike the other two variants in the figure, wherein noticeably uniform lithium concentration is achieved through the entire thickness of the cathode.

As was discussed by means of Figure 4, the influence of effective electrical conductivity with changing bulk density on the half-cell potential at a given intensity, is indiscernible in comparison to other factors like increasing mass and reduced porosity. At constant bulk density however, the increase in effective electrical conductivity with increasing intensity in form of tool speed becomes evident, especially at the higher C-Rate 2 C. As a consequence of the resulting change in half-cell potential, the relative lithium distribution in the solid region of the half-cell is altered, as shown in Figure 6a. It can be seen with the help of the variant CB35, that at a higher effective electrical conductivity in the half-cell a more uniform lithiation takes place. This is because of the ability of the variant at the higher intensity ( $25 \text{ ms}^{-1}$ ) with higher electrical conductivity to conduct electrons through the entire thickness of the cathode leading to a more uniform distribution of the intercalation current, while the variant at the lower intensity ( $20 \text{ ms}^{-1}$ ) leads

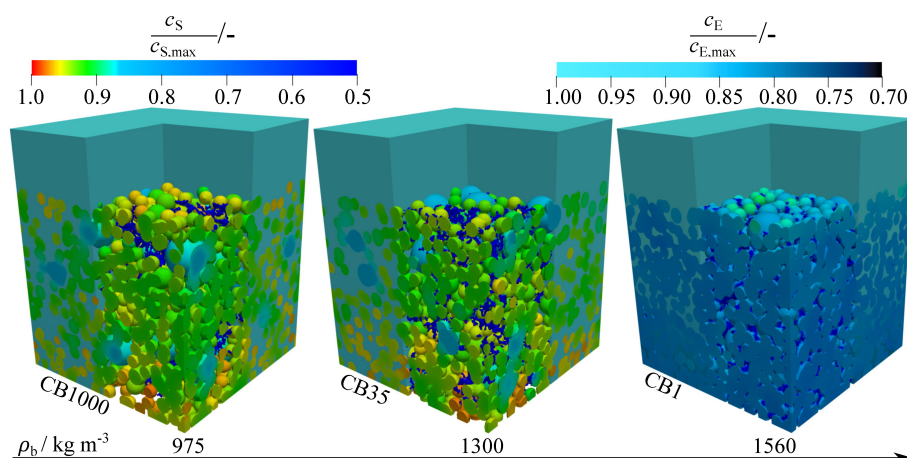


**Figure 5.** Relative lithium concentration distribution in the half cell variants at tool speed  $25 \text{ ms}^{-1}$ . The electrolyte domain is opened up to reveal the cathode surface. The instance represents the end stages of discharge at 0.5 C at an identical DOD 0.84. Solid concentration is shown on the top left and electrolyte concentration on the top right.

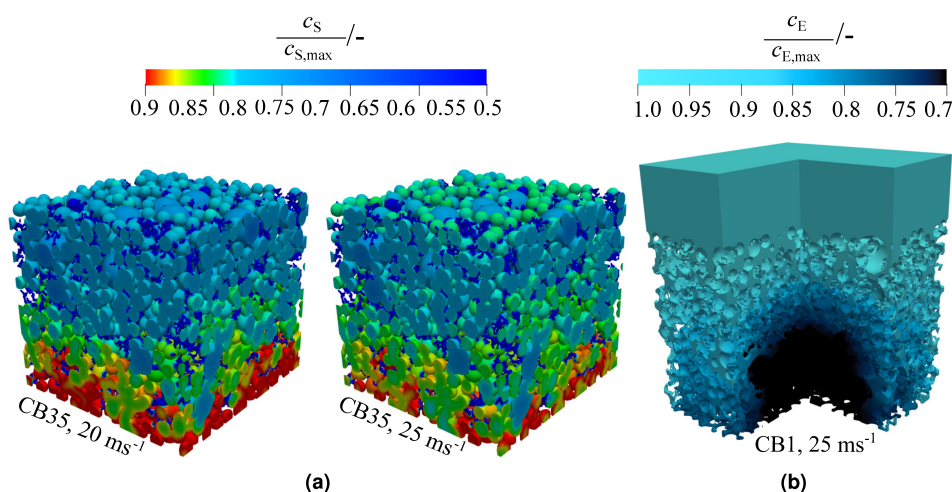


**Figure 6.** Analysis of the resolved lithium concentration distribution at C-Rate 2 C. a) Influence of changing conductivity with intensity at same DOD 0.66, in the solid region. b) Lithium depletion caused by the narrow pores of the CB1 variant at DOD 0.08, in the electrolyte region.

to an accumulation of lithium close to the source of the electrons i.e. the current collector, due to a gradient in the intercalation current that develops in the direction of the electrical current due to the high over-potential caused by the ohmic losses.

Another transport phenomenon in the half-cell that gains significance at higher currents can be explained with the help of the CB1 variant at tool speed  $25 \text{ ms}^{-1}$  subjected to a C-Rate of 2 C. As can be seen from Figure 6b, the concentration of lithium in the electrolyte region of the CB1 variant has declined sharply (upto 30% of initial concentration) at very early stages of discharge (DOD 0.08) depicted in black in the figure. This is due to the low porosity of the variant which leads to very narrow pores. Since the movement of the lithium ions from the anodic sources is restricted in these pores and the diffusion in the solid region is much slower as compared to the electrolyte, the only available source of lithium for the intercalation reaction in the black region from the figure is the lithium in the nearby electrolyte. Consequently, the lithium in the electrolyte in narrow pores is consumed faster than it can be replenished by the ionic flux from the anode, leading to its depletion. Since, the intercalation reaction scales with the C-rate this phenomenon is more prominent at the higher C-Rate (2 C) investigated in this study. Such regions of depletion heavily constrain the half-cell capacity and are suspected to be the cause of early failure of the numerical simulation for the CB1 variant at 2 C in Figure 4a and 4b. A similar depletion of electrolyte was not observed for the remaining variants owing to better quality of pore network in these variant as suggested by the tortuosity (Figure 3b) and porosity (Table 1). In sum, the analysis of the resolved lithium concentration distribution highlights the capacity restricting mechanisms and shortcomings of the investigated variants. However, it cannot be conclusively stated which variant performs the best solely based on this analysis.

### 3.4. Performance Evaluation: Performance Determinants

The indicators of performance discussed until now are insufficient for the comparison of the variants across changing bulk density and intensity as was indicated in Section 2.3 and discussed previously. In order to ensure comparability, the results obtained for the half-cells were modified to correspond to the same cell volume in a volumetric approach as well as to the same mass of the active material in a gravimetric approach similar to the methodology applied by Cernak et al. to compare porous active material particles.<sup>[37]</sup> In doing so, performance determinants that dictate cell performance namely utilizable energy density and utilizable power density were evaluated under the consideration of the respective modification (see Section 2.3).

#### 3.4.1. Utilizable Energy Density

The results of the evaluations concerning energy density have been presented in Figure 7. In this figure, the normalized value of UED evaluated following the respective approaches have been plotted against the bulk density of the variants. The normalization was carried out using the highest achieved UED for a given C-Rate. The absolute values evaluated have been additionally documented in the Supporting Information of the article. From Figure 7a following the volumetric approach, it can be seen that at the lower C-Rate (0.5 C) the UED increases with increase in the bulk density irrespective of the intensity (dotted lines). This is due to the fact that with increasing amount of the active material in the same volume with increasing bulk-density, the theoretical capacity of the half-cell increases. Hence, it can be inferred that at the lower current the transport limitation highlighted previously in the CB1 variant are overcome by the increased theoretical capacity leading to the increased energy density. On the other hand, at the higher C-Rate (2 C), the transport limitations dominate, such that the

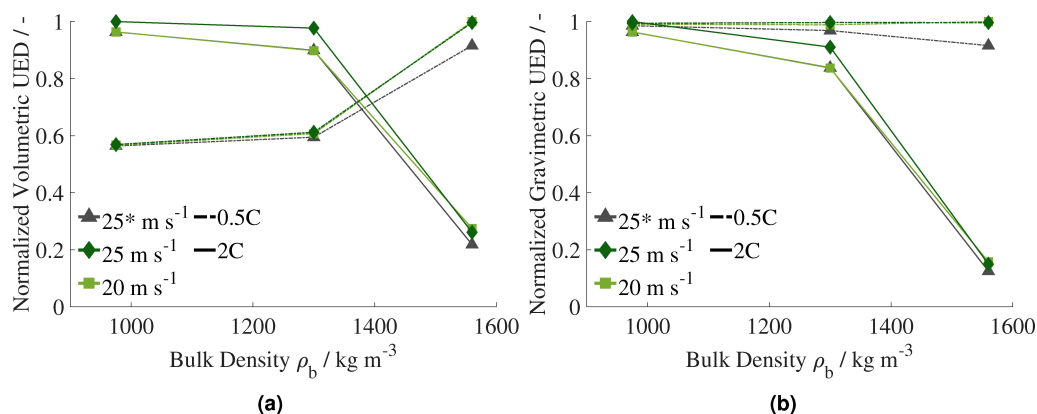


**Figure 7.** Energy density evaluations. a) Volumetric utilizable energy density normalized based on highest value achieved at the respective C-Rate. b) Gravimetric utilizable energy density normalized based on highest value achieved at the respective C-Rate.

reduced porosity of the highest bulk density variant CB1 leads to significant diffusion limitation in the half-cell and hence reduces the utilizable fraction of the theoretical energy (solid lines). This leads to an opposite trend in the Volumetric UED for the higher C-Rate such that it decreases with increasing bulk density. Furthermore, a decrease in the UED upon accounting for the coating factor can be seen owing to the reduced half-cell potential elaborated in the discussion of half-cell potential of the variants. Similarly, the noticeable reduction in the half-cell potential at the higher C-Rate at the same bulk density but different intensity caused by difference in the effective electrical conductivity, leads to lower UED achieved at the lower intensity.

These observations are in accordance with Cernak et al., who observed a shift of the optimum volumetric UED for porous active material particles towards higher porosities with increasing C-Rate. Moreover, in line with the observation made by Cernak et al., it can be argued that the variants in this study ( $975 \leq \rho_b \leq 1560$ ) are limited by theoretical capacity of the bulk at the lower C-Rate (0.5 C) and further increase in the bulk density  $\rho_b > 1560$  would eventually lead to reduction in the volumetric UED as the diffusion limitation starts to dominate owing to the spare pore space. Correspondingly, at the higher C-Rate (2 C) the investigated variants are constrained by the diffusion limitation in the pore space and the UED achievable at even higher porosity is bound to decrease with further decreasing bulk density  $\rho_b < 975$  as the theoretical capacity of the bulk is diminished by the increasing pore space in the same volume.

In contrast, following the gravimetric approach the highest gravimetric UED is always achieved at the lowest bulk density as shown in Figure 7b. In the gravimetric approach, same mass of the active material is taken into consideration hence, the theoretical capacity of the variants is the same. Since the variants with higher bulk density and lower porosity are bounded by diffusion limitation the maximum utilisation of the available capacity of the active material is thus always made at the lowest bulk density irrespective of C-Rate and intensity. It must however be considered that, variants with lower bulk density would occupy more space for the same mass and with

further decrease in the bulk density the available volume for the cell might become limiting. A reduction in the UED for lower intensity and with consideration of the coating factor was also observed for the gravimetric approach as can be seen from the figure.

### 3.4.2. Utilizable Power Density

In Figure 8, the results of the evaluations concerning power density have been presented. In this figure, the normalized value of UPD evaluated following the respective approaches have been plotted against the bulk density of the variants. The normalization was carried out using the highest achieved UPD for a given C-Rate. As was case for the energy density, the absolute values evaluated have been additionally documented in the Supporting Information of the article. From Figure 8a it can be seen that power density of the variants rises with increasing bulk density irrespective of the intensity and C-Rate. When same volume of the cell is considered in the volumetric approach, the increased amount of active material with rising bulk density leads to an increase in the current flowing through the current collector (see Equation 13). The power attained by a half-cell is a product of the current and voltage at the current collector hence, it can be inferred that at a given intensity the increase in current with the bulk density at constant volume overcomes the loss in potential due to the rising over-potential (elaborated in the discussion of Figure 4). However, when the intensity decreases at the lower C-Rate (0.5 C), a reduction in power (indicated by the dotted lines) at the same bulk density occurs due to the lower half-cell potentials achieved at lower intensity. Additionally, accounting for the coating factor helps elucidate the decline in power at tool speeds of  $20 \text{ m s}^{-1}$  and  $25^* \text{ m s}^{-1}$  at constant bulk density in the figure. In contrast, at the higher C-Rate these differences (solid lines) are diminished due to increased current at the current collector which scales with the C-Rate, overcoming the differences in half-cell potential.

In Figure 8b, the results of the gravimetric approach have been shown. It can be seen from the figure that the gravimetric

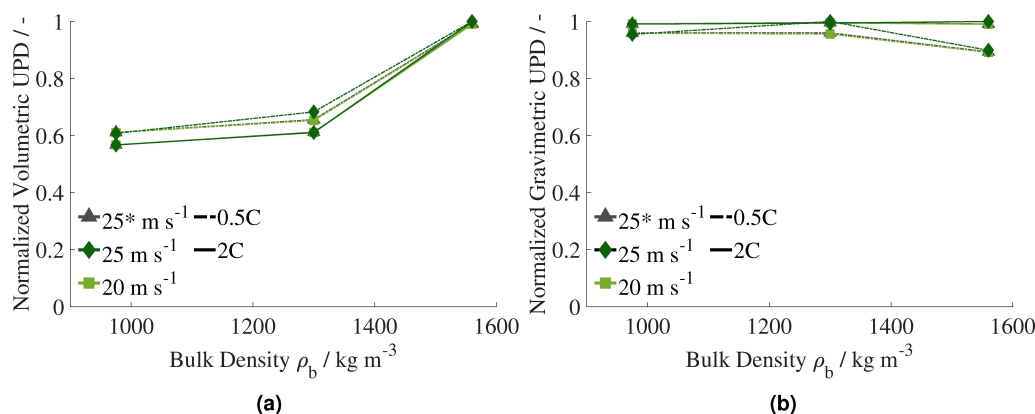


**Figure 8.** Power density evaluations. a) Volumetric utilizable power density normalized based on highest value achieved at the respective C-Rate. b) Gravimetric utilizable power density normalized based on highest value achieved at the respective C-Rate.

UPD remains fairly constant over the C-Rates and changing intensity. This is due to the fact that when equal mass of the active material is considered the current resulting at the current collector for all the variants is the same. In case of the higher C-Rate (2 C) the current completely overcomes the differences in half-cell potential of the variants leading to constant power output over the bulk density, C-Rate and intensity. In contrast, slight changes in the power of the variants at the lower current (0.5 C) can be seen with changing intensity, bulk density and upon consideration of the coating factor arising from the difference in the half-cell potential.

Thus, the dominant factors influencing cell performance in this study were found to be the bulk density and the structural changes resulting from the deagglomeration of carbon black agglomerates for the domain of investigated bulk densities  $975 \leq \rho_b \leq 1560$  and intensities  $20 \text{ m s}^{-1}$  and  $25 \text{ m s}^{-1}$ . Although, the changing intensity via the changing tool speed lead to discernible changes in the half-cell characteristics and potential but its influence of the performance determinants was marginal. Notably, Yonaga et al.<sup>[40]</sup> observed significant changes in the surface coverage of the active material with considerable intensity variation at constant porosity. This variation strongly impacted the intercalation reaction, consequently affecting cell performance and cyclability. However, such a variation in intensity along with the modelling of cyclability was out of the scope of this contribution.

The insights derived from the performance determinants in this study can be distilled into design principles as follows: Adhering to the volumetric approach, thereby limiting the total volume available for the cell. It was found that the variant with the highest bulk density (CB1) exhibited the highest energy density and highest power when considering high energy and low current (0.5 C) applications thereby making it the optimal choice under these operational conditions. At high power application and higher current (2 C) however the lowest bulk density variant (CB1000) showed the highest energy density but poor power density which was highest for the highest bulk density variant (CB1). Thus in case of high current applications where battery volume is the limiting factor one has to settle for a compromise. In case faster dis-/charging and higher power

output is preferred the higher bulk density is more suitable and in applications where the energy output and hence capacity is more critical the lowest bulk density offers the best compromise.

Conversely, if the available volume for the battery is not the limiting factor rather the mass of the active material used in the cell is limiting. The lowest bulk density variant (CB1000) performs the best under high energy (low current) as well as high power (high current) operational conditions. Since at the same amount of material the power output remains the same, the best utilisation of the energy of the lower bulk density variant irrespective of the application type, makes it the clear choice.

In summary, the ideal composition for a given cell hinges on the specific application and limitation on space or material. Additionally, in some instances, prioritizing either energy storage or power delivery in lithium-ion batteries proves crucial due to their intricate interplay.

## 4. Conclusions and Outlook

In this contribution, the emphasis was laid on the impact of intensive dry mixing on the performance of lithium-ion battery cathodes by exploring the attainable microstructural changes. In doing so, the deagglomeration process taking place during such a mixing process was reflected in computationally generated particulate structures by means of a DEM model. The resulting particulate structures were described based on their bulk density. Since the bulk density of a dry blend is an easily measurable parameter, it was used to characterize the mixing process. In this regard, three different variants with bulk densities of active material – carbon black blends representing different stages of comminution of the conductivity additive were generated. Under the consideration of a solvent free manufacturing process the particulate blends were transformed into computational half-cell geometries for the evaluation of their electrochemical performance. The assumption of such a process enabled direct correlation of the microstructure achieved after mixing and resulting cell performance. The

performance of the variants hence generated, were gauged under common battery design considerations and performance determinants. Thereby, at first the volume specific energy density and power density of the variants was evaluated at high energy (lower current 0.5 C) and high power (higher current 2 C) operational conditions.

Followed by mass specific evaluations of the same. It was found that volume specific energy density as well as power density was the highest for the highest bulk density variant (CB1) at the high energy operational condition (0.5 C), due to the increased theoretical capacity as well as the lack of transport limitations at this mode of operation. On the other hand, at the higher current (2 C) the lowest bulk density variant (CB1000) exhibited the highest volume specific energy density while the higher bulk density variant (CB1) delivered the highest volume specific power. The decline in the energy of the CB1 variant was attributed to the transport limitation at the higher current while its higher power output could be clarified by the higher active material mass present in the variant. Hence, it was suggested that such a dilemma over the best blend for this case could only be resolved by a compromise in performance determinants namely, either higher capacity (UED) or fast dis-/charging capability (UPD). The mass specific evaluation in contrast, revealed that the lowest bulk density variant was always the best choice irrespective of the operation condition (C-Rate) and performance determinant. Since the power output for the variant under consideration of same amount of the active material was found to be identical and utilisation of the energy in the CB1000 variant owing to its highly porous microstructure was the highest, it was shown to be the evident choice.

Additionally, within the framework of this publication the influence of changing intensity of the mixing device in terms of changing tool speed along with the coating phenomenon commonly observed for the intensive dry mixing process, were also taken into consideration. While fluctuations in the half-cell potential measured at the current collector were apparent when considering these factors, the alterations in cell performance determinants attributable to these mixing parameters were minimal, especially when compared to the variations associated with changes in bulk density. It is however common knowledge that the coating phenomenon which was also observed in the differences in powder conductivities at the same bulk density among the investigated variants, can have a significant impact on the intercalation reaction at the cathode-electrolyte interface. This in turn is bound to noticeably influence performance at a certain threshold of coating. However, the extent of the influence of coating under various operational conditions and its effects on capacity and dis-/charging capability are yet to be determined. Therefore, the characterization of the coating phenomenon under varying intensities, along with its correlation to performance at the cell level remains a topic of further research.

## Acknowledgements

The authors gratefully acknowledge the funding and support by the German Research Foundation (DFG – Deutsche Forschungsgemeinschaft) within the research training group SiMET under the project number DFG GRK2218/2. Additionally, the support by the state of Baden-Württemberg through bwHPC is highly acknowledged. Further, we thank our colleagues Amadeus Wolf, Felix Gerbig and Nikolai Erhardt for the numerous fruitful discussions. Open Access funding enabled and organized by Projekt DEAL.

## Conflict of Interests

The authors declare no conflict of interest.

## Data Availability Statement

The data that support the findings of this study are available from the corresponding author upon reasonable request.

**Keywords:** solvent-free production · intensive-dry-mixing · conductivity additive · performance

- [1] V. Wenzel, R. S. Moeller, H. Nirschl, *Energy Technol.* **2014**, *2*, Publisher: John Wiley & Sons, Ltd, 176–182.
- [2] M. Weber, R. Moschner, A. Kwade, *Energy Technol.* **2023**, *11*, 2200852.
- [3] Y. Li, Y. Wu, Z. Wang, J. Xu, T. Ma, L. Chen, H. Li, F. Wu, *Mater. Today* **2022**, *55*, 92–109.
- [4] Y. Zhang, S. Lu, Z. Wang, V. Volkov, F. Lou, Z. Yu, *Renewable Sustainable Energy Rev.* **2023**, *183*, 113515.
- [5] F. Frankenberg, M. Kissel, C. F. Burmeister, M. Lippke, J. Janek, A. Kwade, *Powder Technol.* **2024**, *435*, 119403.
- [6] W. Bauer, D. Nötzel, V. Wenzel, H. Nirschl, *J. Power Sources* **2015**, *288*, 359–367.
- [7] H. Bockholt, W. Haselrieder, A. Kwade, *ECS Trans.* **2013**, *50*, 25–35.
- [8] H. Bockholt, W. Haselrieder, A. Kwade, *Powder Technol.* **2016**, *297*, 266–274.
- [9] A. Gyulai, W. Bauer, H. Ehrenberg, *ACS Appl. Energ. Mater.* **2023**, *6*, 5122–5134.
- [10] Z. Chen, Q. Zhang, Q. Liang, *Nanomaterials (Basel Switzerland)* **2022**, *12*, 10.3390/nano12111936.
- [11] H. Li, H. Zhou, *Chem. Commun.* **2012**, *48*, 1201–1217.
- [12] D. Hou, J. Han, C. Geng, Z. Xu, M. M. Al Marzooqi, J. Zhang, Z. Yang, J. Min, X. Xiao, O. Borkiewicz, K. Wiaderek, Y. Liu, K. Zhao, F. Lin, *Proc. Natl. Acad. Sci. USA* **2022**, *119*, e2212802119.
- [13] M. J. Herzog, D. Esken, J. Janek, *Batteries & Supercaps* **2021**, *4*, 1003–1017.
- [14] U. Nisar, N. Muralidharan, R. Essehli, R. Amin, I. Belharouak, *Energy Storage Mater.* **2021**, *38*, 309–328.
- [15] S.-J. Sim, S.-H. Lee, B.-S. Jin, H.-S. Kim, *Sci. Rep.* **2020**, *10*, 11114.
- [16] G. Kaur, B. D. Gates, *J. Electrochem. Soc.* **2022**, *169*, 043504.
- [17] R. Dominko, M. Bele, M. Gaberscek, M. Remskar, D. Hanzel, S. Pejovnik, J. Jamnik, *J. Electrochem. Soc.* **2005**, *152*, A607.
- [18] C. Lischka, S. Gerl, J. Kappes, A. Chauhan, H. Nirschl, *Powder Technol.* **2024**, *431*, 119072.
- [19] A. Chauhan, E. Asylbekov, S. Kespe, H. Nirschl, *Electrochem. Sci. Adv.* **2022**, e2100151.
- [20] S. Burkhardt, M. S. Friedrich, J. K. Eckhardt, A. C. Wagner, N. Bohn, J. R. Binder, L. Chen, M. T. Elm, J. Janek, P. J. Klar, *ACS Energy Lett.* **2019**, *4*, 2117–2123.
- [21] M. Gaberscek, R. Dominko, J. Jamnik, *Electrochem. Commun.* **2007**, *9*, 2778–2783.
- [22] C. Lischka, H. Nirschl, *Energy Technol.* **2023**, *11*, 2200849.

- [23] M. E. Spahr, D. Goers, A. Leone, S. Stallone, E. Grivei, *J. Power Sources* **2011**, *196*, 3404–3413.
- [24] H. Dreger, M. Huelsebrock, L. Froboese, A. Kwade, *Ind. Eng. Chem. Res.* **2017**, *56*, 2466–2474.
- [25] E. Asylbekov, R. Trunk, M. J. Krause, H. Nirschl, *Energy Technol.* **2021**, 2000850.
- [26] F. Hippauf, B. Schumm, S. Doerfler, H. Althues, S. Fujiki, T. Shiratsuchi, T. Tsujimura, Y. Aihara, S. Kaskel, *Energy Storage Mater.* **2019**, *21*, 390–398.
- [27] M. Kespe, M. Gleis, S. Hammerich, H. Nirschl, *Int. J. Energy Res.* **2017**, *41*, 2282–2296.
- [28] A. Chauhan, H. Nirschl, *Energy Technol.* **2023**, 2300281.
- [29] T. M. Inc., MATLAB version: 9.13.0 (R2022b), Natick, Massachusetts, United States, **2022**.
- [30] M. Kespe, H. Nirschl, *Int. J. Energy Res.* **2015**, *39*, 2062–2074.
- [31] G. B. Less, J. H. Seo, S. Han, A. M. Sastry, J. Zausch, A. Latz, S. Schmidt, C. Wieser, D. Kehrwald, S. Fell, *J. Electrochem. Soc.* **2012**, *159*, A697–A704.
- [32] L. S. Kremer, A. Hoffmann, T. Danner, S. Hein, B. Prifling, D. Westhoff, C. Dreer, A. Latz, V. Schmidt, M. Wohlfahrt-Mehrens, *Energy Technol.* **2020**, *8*, 1900167.
- [33] J. Newman, K. E. Thomas-Alyea, *Electrochemical Systems*, 3. Aufl., Wiley-Interscience, s.l., **2012**.
- [34] J. Costard, J. Joos, A. Schmidt, E. Ivers-Tiffée, *Energy Technol.* **2021**, 2000866.
- [35] M. Ecker, T. K. D. Tran, P. Dechent, S. Käbitz, A. Warnecke, D. U. Sauer, *J. Electrochem. Soc.* **2015**, *162*, A1836–A1848.
- [36] M. A. Kespe, Ph.D. thesis, Karlsruher Institut für Technologie (KIT), **2019**, pp. 188.
- [37] S. Cernak, F. Schuerholz, M. Kespe, H. Nirschl, *Energy Technol.* **2020**, 2000676.
- [38] S. Hein, T. Danner, D. Westhoff, B. Prifling, R. Scurtu, L. Kremer, A. Hoffmann, A. Hilger, M. Osenberg, I. Manke, M. Wohlfahrt-Mehrens, V. Schmidt, A. Latz, *J. Electrochem. Soc.* **2020**, *167*, 013546.
- [39] A. C. Ngandjong, A. Rucci, M. Maiza, G. Shukla, J. Vazquez-Arenas, A. A. Franco, *J. Phys. Chem. Lett.* **2017**, *8*, 5966–5972.
- [40] A. Yonaga, S. Kawauchi, Y. Mori, L. Xuanchen, S. Ishikawa, K. Nunoshita, G. Inoue, T. Matsunaga, *J. Power Sources* **2023**, *581*, 233466.

---

Manuscript received: January 25, 2024

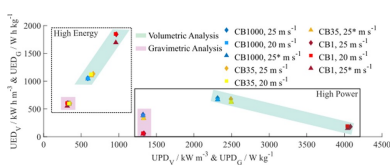
Revised manuscript received: March 11, 2024

Accepted manuscript online: March 20, 2024

Version of record online: ■■, ■■

# RESEARCH ARTICLE

Numerical investigations reveal a significant link between bulk density and cathode performance. Higher bulk density in dry cathode components yields superior performance under low current and high energy conditions, considering limited cell volume. Yet, under high power and current, a balance between energy and power guides selection. Conversely, when material mass constrains, lower bulk density optimally utilizes available energy.



A. Chauhan\*, C. Lischka, H. Nirschl

1 – 16

## Analysis of Solvent-Free Intensive-Dry-Mixed NMC-Based Lithium-Ion Battery Cathodes: Numerical Investigations on Performance Determinants

